RESEARCH ARTICLE

Magnetic Resonance in Medicine

Proton-free induction decay MRSI at 7 T in the human brain using an egg-shaped modified rosette K-space trajectory

Simon Blömer¹ | Lukas Hingerl² | Małgorzata Marjańska³ | Wolfgang Bogner^{2,4} | Stanislav Motyka^{2,4} | Gilbert Hangel^{2,5} | Antoine Klauser⁶ | Ovidiu C. Andronesi^{7,8} Bernhard Strasser²

¹German Center for Neurodegenerative Diseases (DZNE), Bonn, Germany

²High Field MR Centre, Department of Biomedical Imaging and Image-guided Therapy, Medical University Vienna, Vienna, Austria

³Center for Magnetic Resonance Research, Department of Radiology, University of Minnesota, Minneapolis, Minnesota, USA

- ⁴Christian Doppler Laboratory for Clinical Molecular MR Imaging, Medical University Vienna, Vienna, Austria
- ⁵Department of Neurosurgery, Medical University of Vienna, Vienna, Austria
- ⁶Advanced Clinical Imaging Technology, Siemens Healthcare AG, Lausanne, Switzerland
- ⁷A. A. Martinos Center for Biomedical Imaging, Department of Radiology, Massachusetts General Hospital, Charlestown, Massachusetts, USA
- ⁸Harvard Medical School, Boston, Massachusetts, USA

Correspondence

Bernhard Strasser, High Field MR Centre, Department of Biomedical Imaging and Image-guided Therapy, Medical University Vienna, BT32, Lazarettgasse 14, 1090 Vienna, Austria. Email:

bernhard.strasser@meduniwien.ac.at

Funding information

NIH, Grant/Award Numbers: P41EB027061, R01EB031787, R01CA255479; Austrian Science Fund, Grant/Award Numbers: I 6037-1, P 34198, P36328-N

Abstract

Purpose: Proton (¹H)-MRSI via spatial-spectral encoding poses high demands on gradient hardware at ultra-high fields and high-resolutions. Rosette trajectories help alleviate these problems, but at reduced SNR-efficiency because of their k-space densities not matching any desired k-space filter. We propose modified rosette trajectories, which more closely match a Hamming filter, and thereby improve SNR performance while still staying within gradient hardware limitations and without prolonging scan time.

Methods: Analytical and synthetic simulations were validated with phantom and in vivo measurements at 7 T. The rosette and modified rosette trajectories were measured in five healthy volunteers in 6 min in a 2D slice in the brain. An elliptical phase-encoding sequence was measured in one volunteer in 22 min, and a 3D sequence was measured in one volunteer within 19 min. The SNR per-unit-time, linewidth, Cramer-Rao lower bounds (CRLBs), lipid contamination, and data quality of the proposed modified rosette trajectory were compared to the rosette trajectory.

Results: Using the modified rosette trajectories, an improved k-space weighting function was achieved resulting in an SNR per-unit-time increase of up to 12% compared to rosette's and 23% compared to elliptical phase-encoding, dependent on the two additional trajectory parameters. Similar results were achieved for the theoretical SNR calculation based on k-space densities, as well as when using the pseudo-replica method for simulated, in vivo, and phantom data. The CRLBs of γ-aminobutyric acid and N-acetylaspartylglutamate improved non-significantly for the modified rosette trajectory, whereas the linewidths and lipid contamination remained similar.

Conclusion: By optimizing the shape of the rosette trajectory, the modified rosette trajectories achieved higher SNR per-unit-time and enhanced data quality at the same scan time.

KEYWORDS

7 T, gradient hardware restrictions, magnetic resonance spectroscopic imaging, modified rosette trajectory, non-Cartesian trajectory, SNR efficiency

This is an open access article under the terms of the Creative Commons Attribution License, which permits use, distribution and reproduction in any medium, provided the original work is properly cited.

© 2024 The Author(s). Magnetic Resonance in Medicine published by Wiley Periodicals LLC on behalf of International Society for Magnetic Resonance in Medicine.

15222594, 2025, 4, Downloaded from https://onlinelibrary.wiley.com/doi/10.1002/mrm.30368 by Deutsches Zentrum Für Neurodeg, Wiley Online Library on [05/02/2025]. See the Terms and Condi

itions) on Wiley Online Library for rules of use; OA articles are governed by the applicable Creative Commons License

1 | INTRODUCTION

Proton (1H)-MR spectroscopic imaging (MRSI) allows for non-invasive imaging of concentration distributions of the major metabolites in the human brain for (bio)medical applications.^{1,2} MRSI studies at ultra-high field (i.e., >7T) benefit from increased spectral and spatial resolution, as well as an increase in the SNR.³⁻⁶ The most common encoding strategy for MRSI is Cartesian phase encoding. However, this approach suffers from long acquisition times (TAs)⁶⁻⁸ because sampling only along the time-dimension for each k-space point is slow. In contrast, sampling along several k-space dimensions and the time-dimension simultaneously via spatial-spectral encoding (SSE) accelerates data acquisition.^{2,9} Several SSE techniques have been proposed such as echo-planar spectroscopic imaging (EPSI), ^{10,11} spiral-based trajectories, ^{12,13} rosette spectroscopic imaging (RSI),14-17 and concentric ring trajectories (CRT). 18-23 Of these, self-rewinding trajectories such as rosettes and CRT benefit from higher SNR-efficiency at high spatial resolutions and spectral bandwidths because of not needing a rewinding gradient, and therefore, having no acquisition dead time during each circumnavigation of the trajectory. However, they need prewinder and rewinder gradient at the beginning and end of all circumnavigations, therefore, limiting the minimum TE and TR. Hingerl et al.²¹ showed that using a CRT readout at 7 T, eight major neurometabolites could be mapped with high spatial resolution over the majority of the brain with attractive TAs of 3 to 15 min. However, for even higher spatial resolutions or spectral bandwidths, CRT exceeds the limitations of current gradient systems. 24,25 Rosette trajectories are self-rewinding, non-Cartesian alternatives with lower hardware requirements, 14 typically implemented via rosette petals that are distributed around the k-space center. This reduces the maximum petal radius and hence, the required gradient slew rate by half compared to CRT. 14 The reduced gradient stress makes rosette trajectories suitable for application at ultra-high fields and very high spatial resolutions. However, this comes at the cost of an increased TA. To overcome this compressed sensing (CS) techniques have been implemented together with a 3D modified rosette trajectory, benefitting from its incoherent sampling pattern. 26-28 Compared to density-weighted-CRT^{19,20} the rosette trajectory has a reduced SNR efficiency because of unfavorable k-space weighting. Kasper et al.²⁹ showed that SNR can be maximized if no k-space density compensation needs to be performed because the k-space weighting function of a trajectory already matches the desired target weighting (density-weighting). In addition to this SNR improvement, no density compensation during reconstruction is necessary. 19 The increase in SNR is not the result of a difference

in the nominal resolution of two k-space weighting functions, but only the discrepancy between the measured and target k-space densities.^{29–33} Because ¹H-MRSI is often strongly affected by lipid and other nuisance signals, a Hamming weighted k-space is a desirable density function to reduce signal leakage.²⁰ Rosette trajectories deviate substantially from the desired Hamming k-space weighting.

Therefore, we propose an egg-shaped modified rosette trajectory similar to the teardrop trajectory³⁴ that allows for a more SNR-efficient sampling of k-space by changing the shape of the rosette petals. Without any increase in TA and with an adjustable demand on the gradient system, modified rosette trajectories present an enhancement to rosettes and are well-suited for the use at ultra-high field strengths and high spatial resolutions.

2 | METHOD

2.1 | Trajectory design

In contrast to the rosette trajectory that samples the entire k-space along a continuous trajectory, our modified rosette trajectory consists of n individual petals in k-space with radius $k_{\rm max}/2$ and a time varying compression factor (t). It can be written as:

$$k(t) = \begin{pmatrix} k_x \\ k_y \end{pmatrix} = \frac{1}{2} k_{\text{max}} \begin{pmatrix} 1 - \sin\left(\frac{\omega_1 t}{2}\right) \sin\left(\frac{\omega_2 t}{2}\right) \\ e(t) \sin\left(\frac{\omega_1 t}{2}\right) \cos\left(\frac{\omega_2 t}{2}\right) \end{pmatrix} \cdot \mathbf{R}(\alpha)$$
$$(\omega_1 = \omega_2) \frac{1}{4} k_{\text{max}} \begin{pmatrix} 1 + \cos(\omega_1 t) \\ e(t) \sin(\omega_1 t) \end{pmatrix} \cdot \mathbf{R}(\alpha), \tag{1}$$

where $k_{\rm max}=N_x/(2\cdot FoV)$, $\omega_1=\omega_2=\pi SBW/nTi$ with ω_1 and ω_2 being frequencies of oscillation along the radial and angular directions, respectively, nTi is the number of temporal interleaves, and SBW the spectral bandwidth. Please note that for the modified rosette trajectory ω_1 and ω_2 must be equal. The factors $\frac{1}{2}$ and $\frac{1}{4}$ are necessary to cover the whole k-space extent from $-k_{\rm max}/2$ to $+k_{\rm max}/2$ when rotating the trajectory with the rotation matrix ${\bf R}(\alpha)$. The time varying compression factor is described by

$$e(t) = E_1 - (E_1 - E_2)f(t),$$
 (2)

where E_1 , E_2 , are the boundary factors of the compression. f(t) is a function with a range of $0 \le f(t) \le 1$ for $0 \le t \le T$, where T is the time it takes to traverse each individual petal, so that f(t=0) = f(t=T) = 0 and f(t=T/2) = 1. Here, f(t) was chosen as $f(t) = sin(\xi \cdot t/2)$, which results in petals with the boundary compression factors E_1 influencing the compression in the k-space center and E_2 at

15222594, 2025, 4, Downloaded from https://onlinelibrary.wiley.com/doi/10.1002/mrm.30368 by Deutsches Zentrum Für Neurodeg, Wiley Online Library on [05/02/2025]. See the Terms

on Wiley Online Library for rules of use; OA articles are governed by the applicable Creative Commons I

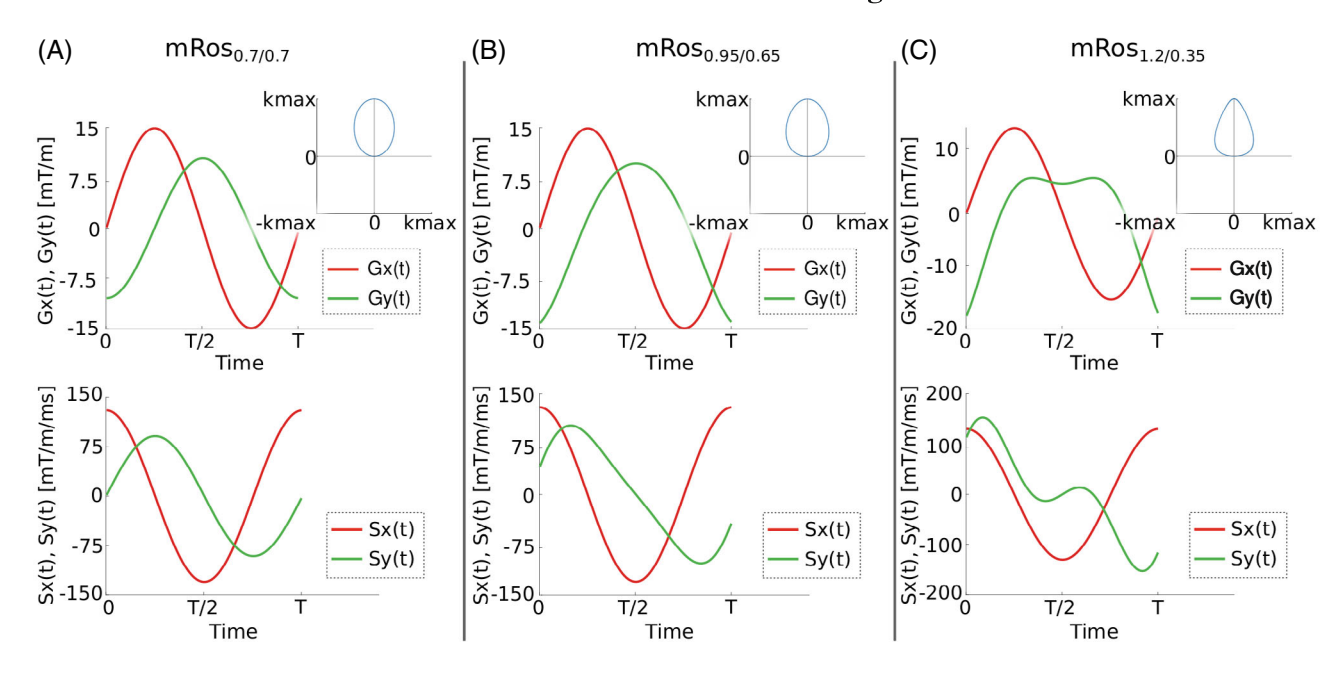


FIGURE 1 k-Space trajectory, gradient amplitudes and slew rate of the modified rosette trajectory for a constant (A) and two sets of time-dependent compression factors (B,C). The gradient moment and slew rate are shown for both phase encoding gradients for one period.

the position $k(T/2) = k_{\text{max}}$. ξ is the modulation frequency of the boundary compression factors and is equal to ω to fulfill the above conditions.

To acquire the entire k-space, each individual petal is rotated around the k-space center with varying angle α using the rotation matrix $\mathbf{R}(\alpha)$ (Figure 1, Figure S1).

With varying boundary compression factors E_1 , E_2 , and function f(t) to transition between them, various petal shapes can be achieved. Using a time-constant compression factor results in elliptical trajectories (Figure 1A). Figure 1B,C shows an "egg-shaped" trajectory that maximizes SNR by best approximating Hamming weighting, while staying within the hardware limitations.

2.2 | k-Space density

Using the two boundary compression factors, the oversampling of the rosette trajectory in the k-space center and k-space periphery can be reduced. This increases the SNR-efficiency since it matches more closely the desired density of a Hamming function. Figure 2 shows the k-space density functions of the rosette and modified rosette trajectories for a 1D line going through the k-space center. Boundary compression factors >1 in the k-space center reduce oversampling because larger circle radii result in a smaller density of sampling points. In the k-space periphery, the desired lower k-space weighting can be achieved using small circle radii. Here, a boundary compression factor <1 should be used.

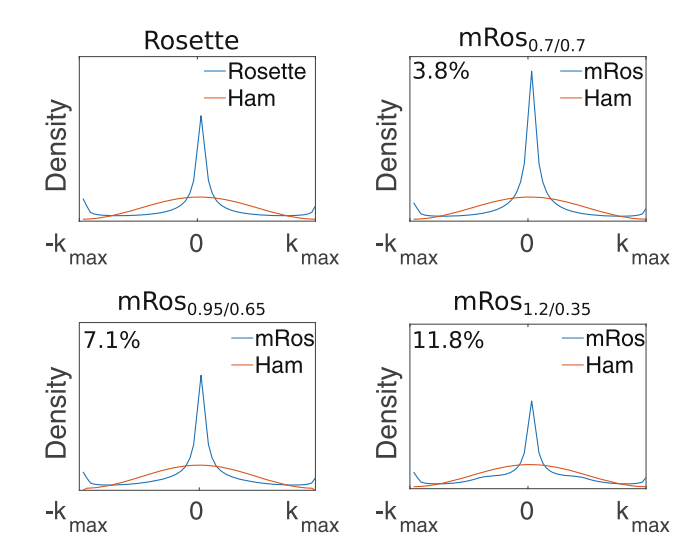


FIGURE 2 k-Space density function of the rosette and modified rosette trajectories for a one-dimensional line with $k_y = 0$ going through the k-space center. The k-space densities of the rosette, mRos_{0.7/0.7}, mRos_{0.95/0.65}, and mRos_{1.2/0.35} trajectories are shown. The relative SNR of the modified rosette trajectories to the rosette trajectory is written on the top left of each subfigure.

2.3 | Gradient amplitude and slew rate

The function e(t) also influences the gradient amplitude and slew rate. For a given spatial resolution and spectral bandwidth, the gradient amplitude and slew rate are minimized if a constant e(t) = 1 is applied. For non-constant e(t), they strongly depend on the difference

15222594, 2025, 4, Downloaded from https://onlinelibrary.wiley.com/doi/10.1002/mrm.30368 by Deutsches Zentrum Für Neurodeg, Wiley Online Library on [05/022025]. See the Terms and Conditions (https://onlinelibrary.wiley. litions) on Wiley Online Library for rules of use; OA articles are governed by the applicable Creative Commons License

 $E_1 - E_2$. The boundary compression factors were optimized for highest SNRs with the help of the simulations described in the following sections while staying within the gradient hardware restrictions. For the measurement parameters described later, the resulting trajectories had maximum gradient amplitudes of 14.9 mT/m, 14.9 mT/m, 15.1 mT/m, and 17.8 mT/m for the rosette trajectory, and modified rosette trajectories with three different sets of boundary compression factors $(E_1/E_2=0.7/0.7,$ $E_1/E_2=0.95/0.65$, and $E_1/E_2=1.2/0.35$ referred to as $mRos_{0.7/0.7}$, $mRos_{0.95/0.65}$, and $mRos_{1.2/0.35}$), respectively. The maximum gradient slew rates for the same trajectories were 130.1, 130.1, 143.9, and 191.9 mT/ms/m, respectively. All trajectories were calculated for the same parameters such as spectral bandwidth, number of angular and temporal interleaves, spatial resolution (see point 3.5 for the exact values).

2.4 | Simulations

Kasper et al.²⁹ showed that the SNR of a measurement is maximized when the k-space density function matches the desired target function. Therefore, when choosing a Hamming filter, the SNR-efficiency of a trajectory can be calculated via the SNR ratio to a hypothetical Hamming filter:

$$\frac{\text{SNR}_{\text{Acq}}}{\text{SNR}_{\text{Hamming}}} = \sqrt{\frac{\sigma_{\text{Hamming}}^2}{\sigma_{\text{Acq}}^2}},$$
 (3)

where $\sigma_{\rm Hamming}^2$, $\sigma_{\rm Acq}^2$ are the noise variance of the Hamming and acquired k-space weighting. The noise variance was calculated from the k-space density function simulated using the acquisition parameters. ²⁹ We calculated the percentage deviation of the SNR of the modified rosette trajectories to the rosette trajectory, as well as to phase encoding and EPSI with ramp sampling. In addition to this analytical approach, the SNR was evaluated by simulating artificial k-spaces using the reconstruction matrix from the in vivo measurements and applying the pseudo multiple replica-based SNR calculation³⁵ after reconstruction (see point 3.6 for more information). Here, the percentage deviation of the SNR of the modified rosette trajectories to the rosette trajectory was calculated.

2.5 | Experiments

Data were acquired on a 7T MAGNETOM+ (Siemens Healthineers AG) with a 32-channel RF head coil for receive, and a volume coil for receive and transmit (Nova Medical) from a silicon oil and resolution phantom and seven healthy volunteers. Written informed consent was

obtained from all volunteers. Three of the seven volunteers were measured twice.

In addition to the modified rosette trajectories with three different sets of boundary compression factors (mRos_{0.7/0.7}, mRos_{0.95/0.65} and mRos_{1.2/0.35}), the rosette trajectory was measured. The following parameters were used for both the phantom and in vivo measurements for all trajectories: matrix size 64×64 , FOV $220 \times 220 \text{ mm}^2$, slice thickness 10 mm, resolution $3.4 \times 3.4 \times 10$ mm³, two temporal interleaves, 840 FID points, spectral bandwidth 2778 Hz, ADC bandwidth 666.666 kHz (considering oversampling), and oversampling factor 2. All of the compared trajectories share the same trajectory parameters (i.e., 101 petals, 72 gradient points per petal, 240 ADC points per petal, k_{max} 0.145 mm⁻¹, spectral bandwidth 2778 Hz). Two in vivo scans were obtained, one with WET water suppression, four averages and TR 440 ms, TE 1.1 ms, TA 6:04 min:s, and the other without water suppression, one average and TA 1:31 min:s for estimating the coil combination weights. The latter settings were also used for the phantom measurements. Five volunteer were measured for these comparisons.

Five volunteers were measured using the mRos_{1.2/0.35} trajectory and an elliptical phase-encoding sequence in an additional session. While the mRos_{1.2/0.35} trajectory was measured with the parameters described above the following parameters were used for the elliptical phase-encoding sequence: matrix size 64×64 , FOV 220×220 mm², slice thickness 10 mm, resolution $3.4 \times 3.4 \times 10$ mm³, 2048 FID points, spectral bandwidth 4200 Hz, and oversampling factor 2. Two in vivo scans were obtained, one with WET water suppression, one averages and TR 440 ms, TA 22:02 min:s, and the other without water suppression, one average and TA 2:30 min:s for estimating the coil combination weights.

The four trajectories were estimated based on oil phantom measurements using an adapted method of Brodsky et al. 36 and Robison et al. 37 by measuring the phase effect of each gradient using thin slices orthogonal to the investigated gradient with negative and positive slice offsets and negative and positive gradient polarities. We used the same parameters as for the in vivo measurements, except: slice thickness 1 mm, slice offsets of 20 mm, TE 6.02 ms, and using the volume coil for signal reception.

A 3D-T₁-weighted magnetization prepared rapid gradient echo (MP2RAGE)³⁸ sequence was measured in the in vivo scan protocol for anatomical reference with a nominal resolution of $1.1 \times 1.1 \times 1.2$ mm³ and TA of 4:57 min:s. 3D FID-MRSI scans using the mRos_{1.2/0.35} were measured, once with water suppression, and once without. The following parameters were used: matrix size $64 \times 64 \times 17$, FOV $220 \times 220 \times 76$ mm³, two temporal interleaves, 840 FID points, spectral bandwidth 2778 Hz, one average, TR

440 ms, and TA 18:44 min:s. Note that the acquisition of the coil combination weights can be highly accelerated, but this was not the purpose of this paper. Before the measurements, manual shimming was performed. MRSI data were filtered to a Hamming weighting in k-space, and reconstructed with a type 2 non-uniform discrete Fourier transform using the measured trajectories. A lipid removal using an L1-regularization was performed.³⁹

2.6 | Evaluation

In vivo spectra were fitted using LCModel (Figure S2).⁴⁰ Our basis set included 17 simulated brain metabolites and a measured macromolecular background.41 SNR per-unit-time ratios were calculated for all volunteers and trajectories using the pseudo replica method. The noise was estimated for each voxel using the SD through a stack of pseudo replicas of the true image with added, uniformly distributed, and correctly scaled noise. This is a simulation-equivalent of measuring multiple times the same data, and was shown to provide good estimate for the SD of the noise.²⁹ The signal was defined as the amplitude of the fitted NAA peak. 42 A mean over all voxels inside a brain mask derived from the T₁-weighted images was calculated. The mean and standard error over all volunteers is reported. The same comparison is performed for the Cramer-Rao lower bounds (CRLB) values of NAA, total creatine (tCr), total choline (tCho), glutamate (Glu), myo-inositol (myo-Ins), N-acetylaspartylglutamate (NAAG), glutathion (GSH), and γ-aminobutyric acid (GABA), the spectral linewidth, and the lipid SNR. The CRLBs and linewidths are calculated by LCModel, whereas the lipid SNR was calculated by summing the magnitude spectra in the range of 0.0 to 1.8 ppm and dividing by the SD of the noise. Metabolic maps and spectra are shown for the first volunteer in agreement with minimum reporting standards⁴³ (Table S1).

Two-sided paired *t* tests were performed to test for statistically significant differences between SNR per-unit-time, linewidth, CRLB, and lipid SNR values of the different modified rosette trajectories to the rosette trajectory.

3 | RESULTS

3.1 | SNR Simulations

The k-space density simulations evaluate to an SNR increases of 3.8%, 7.1%, and 11.8% to the rosette trajectory for the mRos_{0.7/0.7}, mRos_{0.95/0.65}, and mRos_{1.2/0.35} trajectories, respectively. Compared to phase encoding

the simulations showed significant SNR improvements of 16.6%, 20.19%, 24.5% and 32.01%, 36.10%, 42.08% compared to EPSI for the $mRos_{0.7/0.7}$, $mRos_{0.95/0.65}$, and $mRos_{1.2/0.35}$ trajectories, respectively. Using the pseudo multiple replica method on simulated data, percentage increases compared to the rosette trajectory of 2.0%, 2.6%, and 8.7% for the $mRos_{0.7/0.7}$, $mRos_{0.95/0.65}$, and $mRos_{1.2/0.35}$, respectively, were estimated.

3.2 | Phantom results

In Table S2 the calculated SNRs per-unit-time from phantom measurements are reported. For better comparison, the percentage deviation of the mean SNR per-unit-time values calculated over the entire phantom for the modified rosette trajectories to the rosette trajectory is shown. All three modified rosette trajectories showed significantly higher SNRs per-unit-time compared to the rosette trajectory. Over all three measurements the SNR per-unit-time increased in comparison to rosette trajectory by $3.81\% \pm 0.2\%$ ($p \ll 0.001$), $7.00\% \pm 0.17\%$ ($p \ll 0.001$), and $12.47\% \pm 0.29\%$ ($p \ll 0.001$) for the mRos_{0.7/0.7}, mRos_{0.95/0.65}, and mRos_{1.2/0.35} trajectories, respectively. In Figure 3, the reconstructed images from the phantom measurements are shown. No differences can be seen in the images reconstructed with the measured trajectories (Figure 3, bottom row). Using an analytically determined trajectory lead to localization errors near the edges of the phantom when the modified rosette trajectory was used (Figure 3, top row). In Figure S3, the results of the resolution phantom measurement are shown. Similar resolution properties can be observed for the rosette and modified rosette trajectories.

3.3 | In vivo results

Table 1 shows the calculated SNR per-unit-time deviation of the modified rosette trajectories in comparison to the rosette trajectory. Mean SNR per-unit-time gains of 3.0% (p = 0.03), $6.3\% \pm 1.1\%$ (p < 0.03), and $8.9\% \pm 1.6\%$ (p < 0.03) can be observed over all subjects for the mRos_{0.7/0.7}, mRos_{0.95/0.65}, and mRos_{1.2/0.35} trajectories, respectively. Compared to elliptical phase-encoding a mean SNR per-unit-time gain of $21.0\% \pm 4.8\%$ (p < 0.03) was observed. Representative spectra for the first volunteer at a voxel location specified by the minimum reporting standards⁴³ for all compared trajectories are shown in Figure 4. The raw spectra and fitted data are displayed. Good fitting results with similar noise can be observed in the spectra for all trajectories. Reduced noise can be observed in the spectrum measured with the elliptical

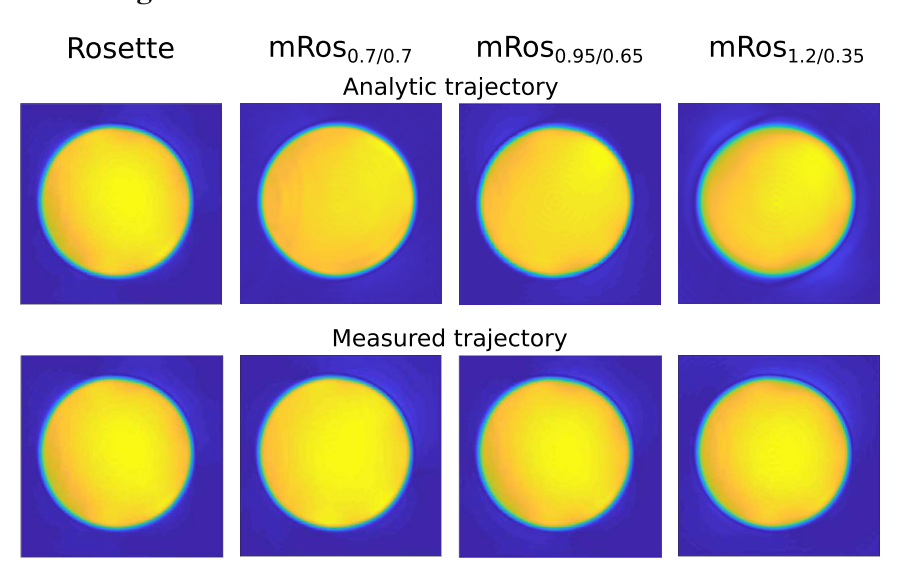


FIGURE 3 Results from the phantom measurement using a silicon oil phantom and the in vivo protocol (FOV of 220 × 220 mm², slice thickness 10 mm, and matrix size of 64×64). The phantom was measured with the rosette, mRos_{0.7/0.7}, mRos_{0.95/0.65}, and mRos_{1.2/0.35} trajectories. The phantom results were Hamming weighted and zero-filled to obtain a matrix size of 300 × 300. Images were reconstructed with an analytically determined (top row) and measured (bottom row) trajectories. Using a measured trajectory eliminated significant artifacts from gradient trajectory errors that can be observed for mRos_{1,2/0,35}.

TABLE 1 Mean and standard error SNR per-unit-time calculated using the pseudo-replica method over all voxels inside an ROI (see Figure 5) for all volunteers and the trajectories with different compression factors.

	Rosette	mRos _{0.7/0.7}	mRos _{0.95/0.65}	mRos _{1.2/0.35}	mRos _{1.2/0.35}	ePE
Vol 1	1.37 ± 0.34	1.42 ± 0.33	1.48 ± 0.34	1.53 ± 0.36	1.54 ± 0.01	1.26 ± 0.01
Vol 2	1.36 ± 0.34	1.41 ± 0.35	1.44 ± 0.36	1.49 ± 0.37	1.62 ± 0.01	1.28 ± 0.01
Vol 3	1.40 ± 0.33	1.44 ± 0.32	1.47 ± 0.33	1.51 ± 0.35	1.54 ± 0.01	1.25 ± 0.01
Vol 4	1.20 ± 0.32	1.26 ± 0.32	1.28 ± 0.32	1.31 ± 0.35	1.68 ± 0.01	1.46 ± 0.01
Vol 5	1.31 ± 0.34	1.31 ± 0.32	1.39 ± 0.35	1.40 ± 0.36	1.42 ± 0.01	1.22 ± 0.01
Mean	1.33 ± 0.08	1.37 ± 0.08	1.41 ± 0.08	1.45 ± 0.09	1.56 ± 0.1	1.29 ± 0.1

Abbreviations: ROI, region of interest; Ros, modified rosette.

phase encoding sequence. Two dimensional metabolic maps (Figure 5) and CRLB maps (Figure 6) for the first volunteer are shown. Hardly any differences between the trajectories are visible for NAA, tCr, tCho, Glu, myo-Ins, and GSH. Using the mRos_{1.2/0.35} trajectory, improved GABA maps were achieved as a result of reduced CRLB values. For NAAG reduced CRLB values and improved maps were observed using the mRos_{0.7/0.7} trajectory. Some maps have more outliers in the front of the brain, which might stem from incorrect coil combination weights. Reduced CRLB values can be observed for the elliptical phase encoding sequence, leading to improved metabolic maps. GABA could not be fitted reliably for the elliptical phase-encoding sequence. In the 3D metabolic (Figure 6) and CRLB (Figure S4) maps, similar fitting results were achieved for all metabolites except NAAG compared to the 2D acquisition. However, the 3D dataset had more ringing artifacts in some metabolic maps, which we believe was because of B₀-inhomogeneities. 2D SNR maps for the first volunteer are shown in Figure 8.

The mean CRLB values of all voxels with CRLB<50% for NAA, tCr, tCho, Glu myo-Ins, NAAG, GSH, and

GABA are shown in Figure 9. Most voxels inside the brain mask (Figure 5) had CRLBs <50% for all metabolites except NAAG. Similar means can be observed for the rosette and modified rosette trajectories for all metabolites except GABA and NAAG. Across all volunteers the mRos_{1.2/0.35} shows lower mean CRLBs than the other trajectories. Similarly, the mRos_{0.7/0.7} has lower mean CRLBs than the other trajectories for NAAG. An increase of the number of voxels with CRLB values below 20% is observed for the mRos_{1,2/0,35} for GABA and mRos_{0,7/0,7} for NAAG compared to the rosette trajectory. The linewidths were $14.24 \pm 0.1 \,\text{Hz}$, $14.25 \pm 0.1 \,\text{Hz}$, $14.27 \pm 0.1 \,\text{Hz}$, and $14.38 \pm 0.1 \,\mathrm{Hz}$ for the rosette, mRos_{0.7/0.7}, mRos_{0.95/0.65}, and mRos_{1,2/0,35} trajectories, respectively. The lipid SNR normalized to the rosette values were 1.00 ± 0.10 , 0.79 ± 0.036 , 1.16 ± 0.05 , and 1.07 ± 0.05 . Paired t tests between the values of the modified rosette trajectories and the rosette showed that the CRLB, linewidth, and lipid SNR are non-significantly different. The mean CRLB values of the mRos_{1,2/0,35} trajectory normalized to elliptical phase-encoding for NAA, tCr, tCho, Glu, myo-Ins, NAAG, GSH, and GABA were 1.09 ± 0.02 (p < 0.02),

15222594, 2025, 4, Downloaded from https://onlinelibrary.wiley.com/doi/10.1002/mrm.30368 by Deutsches

¿Zentrum Für Neurodeg, Wiley Online Library on [05/02/2025]. See the Terms

s of use; OA articles are governed by the applicable Creative Commons

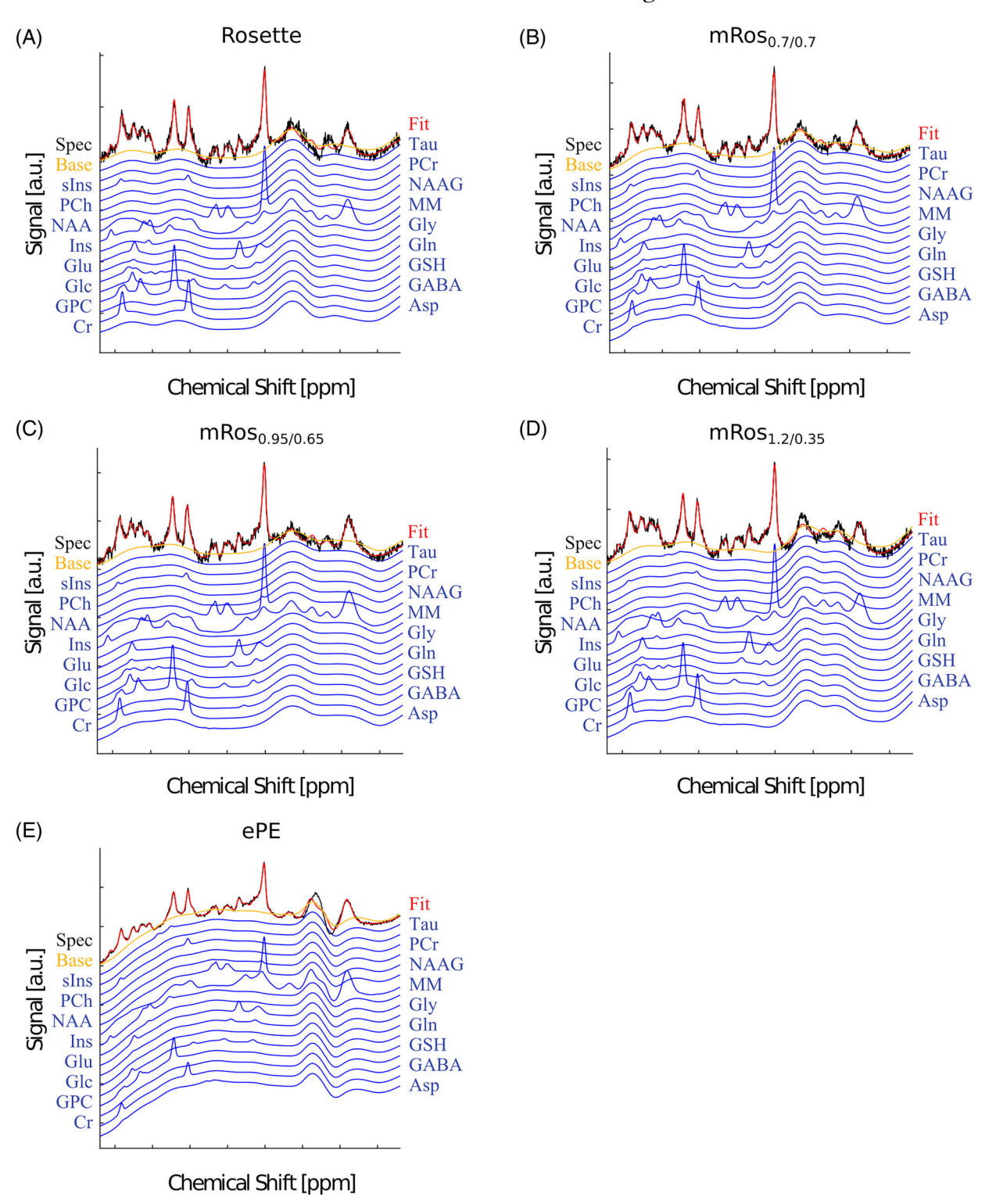


FIGURE 4 In vivo spectra from the first volunteer and all measured trajectories (rosette [A], mRos_{0.7/0.7} [B], mRos_{0.95/0.65} [C], mRos_{1.2/0.35} [D], and elliptical phase-encoding [E]). Fitted spectra (red) and measured data (black) were taken from LCModel. First order phase correction was performed. Similar spectral noise can be observed for the spectra acquired with the rosette, mRos_{0.7/0.7}, mRos_{0.95/0.65}, and mRos_{1.2/0.35} trajectories. The voxel location from which the spectra are taken is shown in Figure 5.

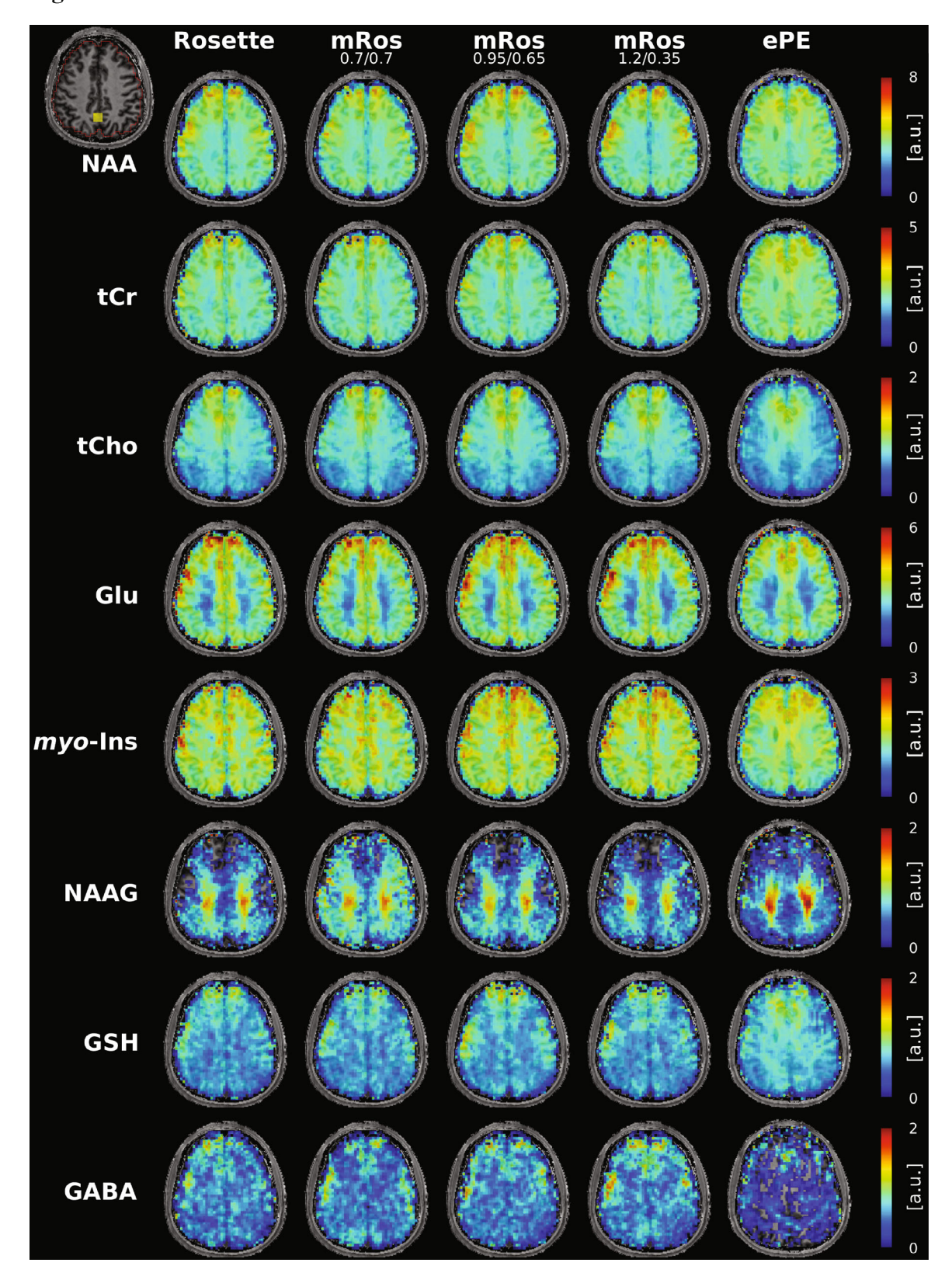


FIGURE 5 Results from the first volunteer using the rosette, $mRos_{0.7/0.7}$, $mRos_{1.2/0.35}$ and $mRos_{0.95/0.65}$ trajectory and elliptical phase-encoding (FOV of 220×220 mm², slice thickness 10 mm and matrix size of 64×64). Metabolic maps for NAA, total creatine (tCr), total choline (tCho), glutamate (Glu), myo-inositol (myo-Ins), N-acetylaspartylglutamate (NAAG), glutathion (GSH), and γ -aminobutyric acid (GABA), are displayed. The region of interest (ROI) and voxel location of the spectra shown in Figure 4 is shown in the top left.

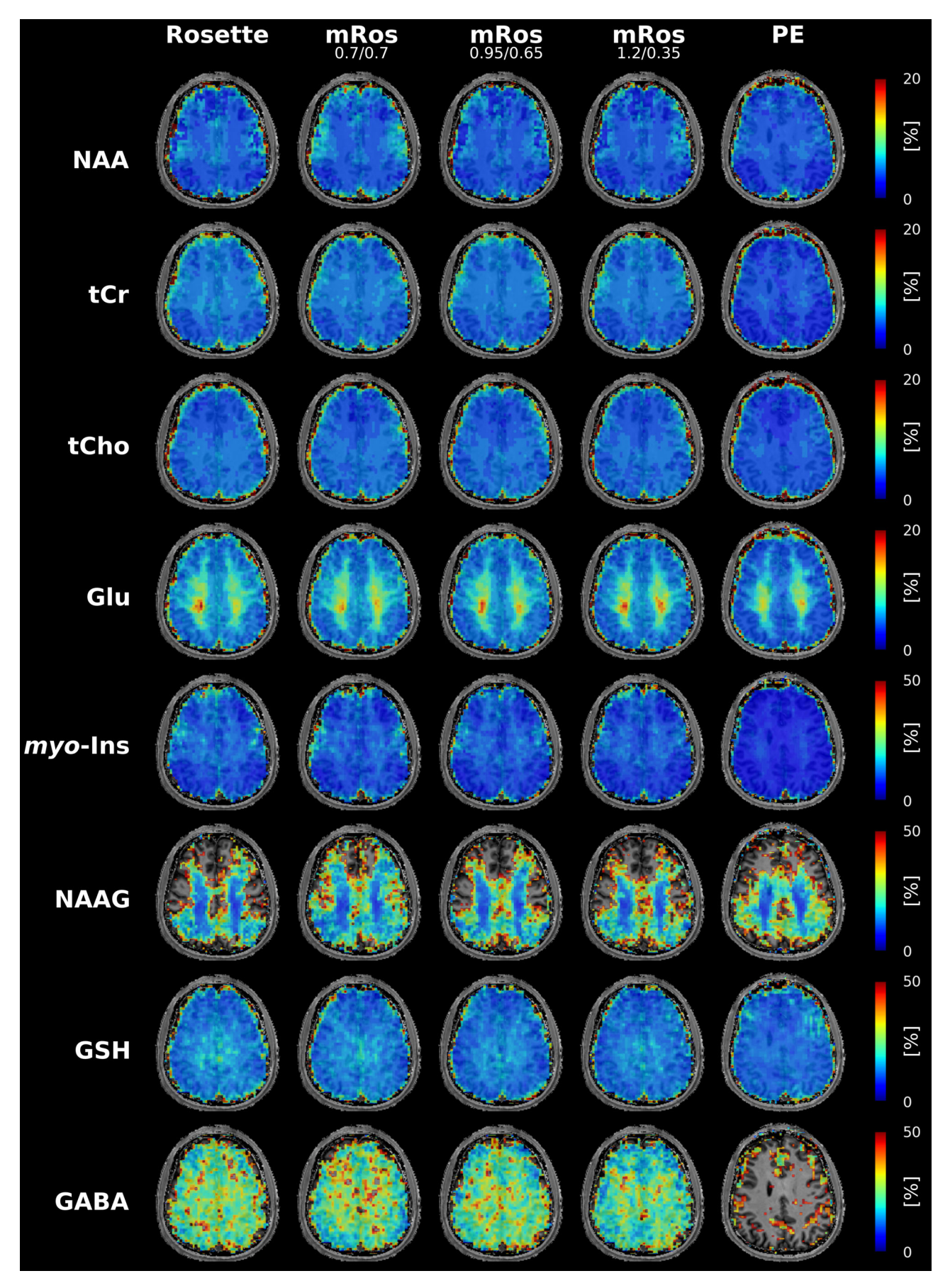


FIGURE 6 Cramer-Rao lower bounds (CRLB) maps for the metabolites shown in Figure 5. CRLB values were taken from LCModel.

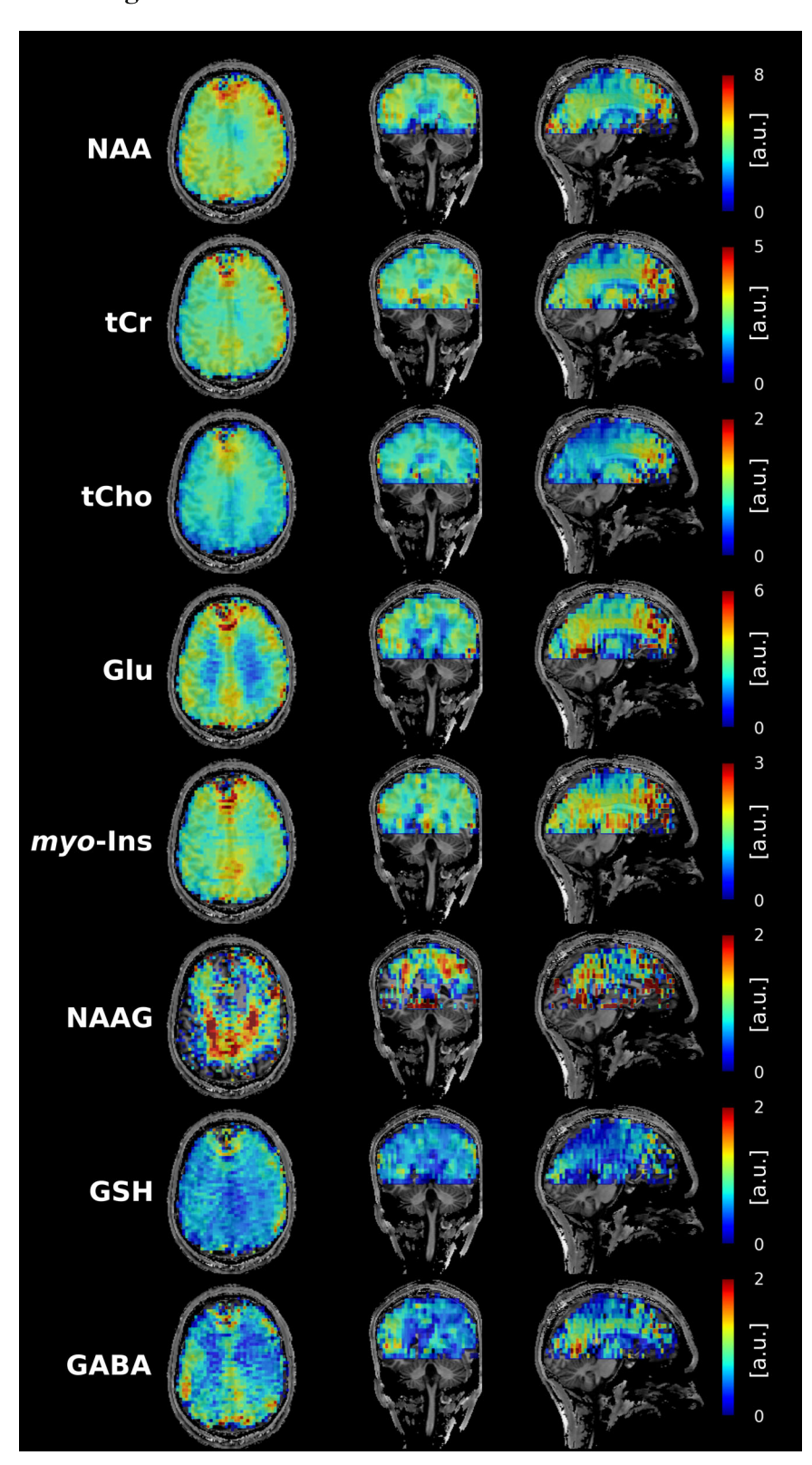


FIGURE 7 Whole-brain metabolic maps acquired with the mRos_{1.2/0.35} trajectory. A matrix size of $64 \times 64 \times 17$ was measured in 19 min.

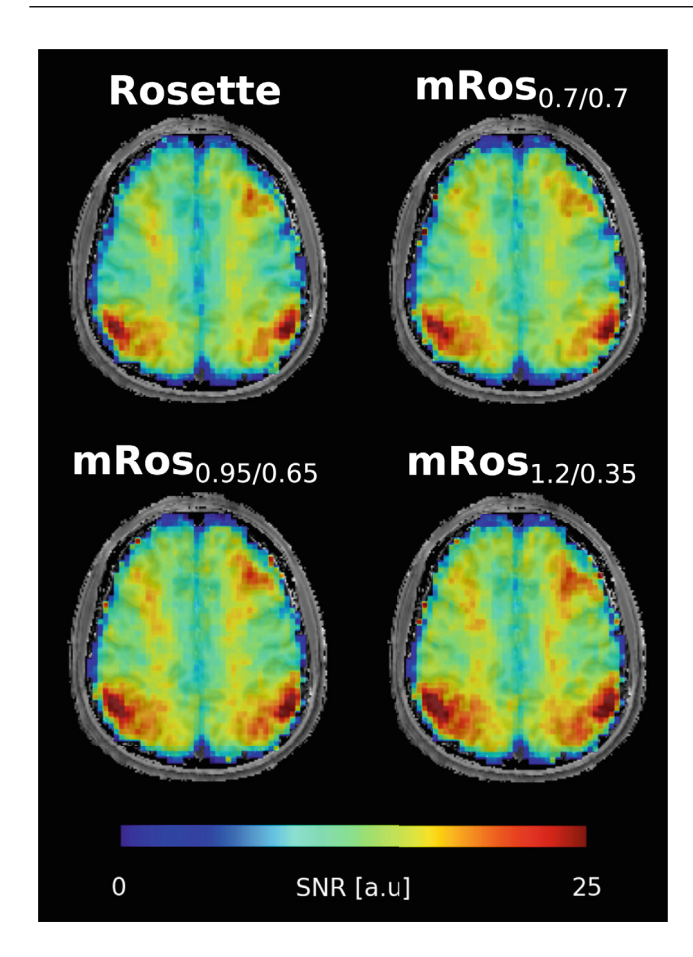


FIGURE 8 SNR maps from the first volunteer for the rosette and modified rosette trajectories.

 1.29 ± 0.02 (p < 0.01), 1.2 ± 0.02 (p < 0.02), 1.23 ± 0.03 (p < 0.02), 1.4 ± 0.03 (p < 0.01), 1.05 ± 0.04 (p = 0.4), 1 ± 0.01 (p = 0.7), and 1 ± 0.04 (p < 0.01), respectively. The linewidths were 14.42 ± 0.09 for mRos_{1.2/0.35} and 12.78 ± 0.09 for elliptical phase-encoding (p < 0.03). The lipid SNR of the mRos_{1.2/0.35} trajectory normalized to elliptical phase-encoding was 1.21 ± 0.02 (p < 0.03).

4 | DISCUSSION

We have shown that by modifying the rosette trajectory higher SNR per-unit-time values of up to +12% can be achieved. The SNR per-unit-time results from phantom and in vivo measurements were consistent with simulations, but a smaller SNR per-unit-time increase was observed in the in vivo data using the mRos_{1.2/0.35} trajectory (Figure S5). The reason for that might be that this trajectory is more susceptible to subject related artifacts such as motion. The highest SNR per-unit-time was achieved with the mRos_{1.2/0.35} (\sim 9% higher than rosette), followed by the mRos_{0.95/0.65} (\sim 6% higher than rosette) and mRos_{0.7/0.7} (\sim 3% higher than rosette), whereas the

lowest SNR per-unit-time was achieved with rosette trajectory. Because of the similar design of the trajectories and the same number of sampling points along the trajectory, no additional measurement time is necessary to realize this SNR per-unit-time gain. Compared to elliptical phase-encoding the $mRos_{1.2/0.35}$ achieved a ~21% increase in SNR per-unit-time, which is consistent with the first simulation. All compared trajectories had similar linewidths, lipid contaminations, and resolution properties. The non-significant decrease of the mean CRLBs for GABA of the modified rosette data in comparison to the rosette data indicate that the SNR per-unit-time increase leads to a small improvement in metabolite quantification precision for low-concentration metabolites. The mRos_{0.7/0.7} trajectory showed improved NAAG maps and reduced CRLBs compared to the other trajectories, despite lower SNR per-unit-time than the other modified rosette trajectories. The reason for this remains unknown. The increase in measurement time of the elliptical phase encoding sequence lead to a reduction in most CRLBs and linewidths while the lipid SNR increased slightly.

Kasper et al.²⁹ and several others showed that the sampling SNR-efficiency is highest, when the measured k-space density matches the desired k-space density. 31-33,44 This can be understood intuitively: Measuring data with matched density focuses on important regions allowing to average more data there, and avoiding unnecessary noise from less important areas. In contrast, rescaling the data in postprocessing rescales signal and noise exactly the same. It is important to understand that with a "desired k-space density" we mean to achieve this density in postprocessing by compensating any remaining discrepancies between the measured and desired density. Our desired k-space density was a Hamming filter, which is reasonably well approximated by modified rosette trajectories, and less so by rosette trajectory. However, despite this closer approximation to Hamming weighting, density filtering is still required before reconstruction for all trajectories. Both, the rosette and modified rosette trajectories have mild oversampling of the k-space center. This comes at the disadvantage of less efficient k-space sampling and a greater deviation from the ideal k-space weighting. However, mild oversampling of the k-space center makes the trajectories more robust against subject motion as shown by Schirda et al. 14

The slew rate of the $mRos_{1.2/0.35}$ trajectory of 191.9 mT/ms/m was close to the hardware limit of 200 mT/ms/m and noticeably higher compared to that of the rosette and $mRos_{0.7/0.7}$ trajectories, which used 130.1 mT/ms/m. Measurements with the $mRos_{0.95/0.65}$ trajectory resulted in a \sim 6% SNR per-unit-time increase. With maximum slew rates of 143.9 mT/ms/m, which are slightly higher than those of the rosette, the $mRos_{0.95/0.65}$ trajectory can be a

1522.2594, 2025, 4, Downloaded from https://onlinelibrary.wiley.com/doi/10.1002/mrm.30368 by Deutsches Zentrum Für Neurodeg, Wiley Online Library on [05/02/2025]. See the Terms and Conditions (https://onlinelibrary

on Wiley Online Library for rules of use; OA articles are governed by the applicable Creative Commons!

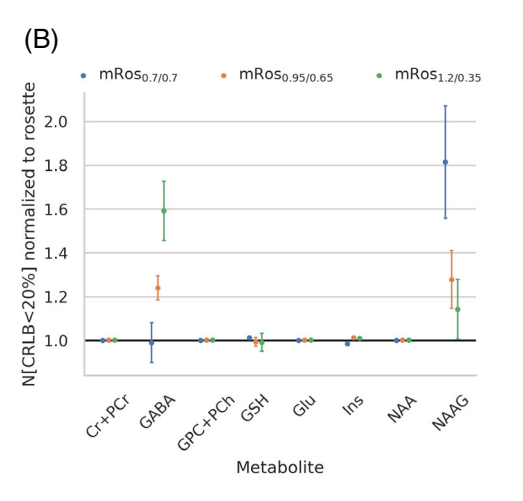


FIGURE 9 Mean of the Cramer-Rao lower bounds (CRLBs) over all voxels inside the brain with CRLB <50% for NAA, total creatine (tCr), total choline (tCho), glutamate (Glu), myo-inositol (myo-Ins), N-acetylaspartylglutamate (NAAG), glutathion (GSH), and γ-aminobutyric acid (GABA). The number of voxels with CRLB <20% are shown for the same metabolites.

good compromise between high SNR per-unit-time and reduced gradient stress.

A major advantage of modified rosette trajectories is the flexibility to adjust the two compression factors so that a given slew rate restriction is met, whereas maximizing the SNR per-unit-time. By doing so, the sequence can be adapted for several different modalities, such as different magnetic field strengths or matrix sizes. The smallest achievable slew rate is that of the rosette trajectory. All compared trajectories provided similar spectra and metabolic maps, indicating comparable spectral qualities between all trajectories.

In comparison to other SSE trajectories, such as spiral and EPSI trajectories, modified rosette trajectories benefit from their self-rewinding properties. This provides higher SNR because of not needing a rewinder gradient. Moreover, the k-space density of modified rosette trajectories is closer to a Hamming filter than most other MRSI trajectories, except the ideally shaped density-weighted CRT sampling.^{19,20} Modified rosette trajectories achieve their k-space density not by measuring additional angular interleaves as is the case for density-weighted CRT, but by changing the gradient shape. Therefore, the modified rosette trajectories do not prolong the measurement while achieving a comparable SNR-efficiency as density-weighted CRT encoding. In addition, the modified rosette trajectories, as well as the rosette use smaller circles than CRT, and therefore, can cover much higher spectral bandwidths for a given resolution, which is essential for MRSI at >7 T¹⁴. For example, using the in vivo parameters (2778 Hz SBW, 3.4 mm in-plane resolution, 2 temporal interleaves, TR 440 ms, maximum slew rate of 192 mT/m/ms) CRT or EPSI with ramp-sampling is not possible. However, EPSI with ramp-sampling can be done with a similar SBW of 2667 Hz, but the SNR-efficiency in comparison to a Hamming filter drops to only 57% (for comparison: rosette: 79%, mRos_{1,2/0,35}: 89%).

The measurement time for the 3D protocol would be 15:57 min:s. CRT can only achieve similar parameters with three temporal interleaves, resulting in 8:56 min:s measurement time for the 3D protocol, and an SNR-efficiency of 91.72%. However, at an in-plane resolution of 1.7 mm or spectral bandwidth of 3840 Hz (e.g., for 9.4 T measurements), even three temporal interleaves are not enough for CRT, whereas it is still possible to measure the modified rosette trajectories with three temporal interleaves. Increasing the number of temporal interleaves even further is not feasible because it causes spectral artifacts.²⁰ Modified rosette trajectories share the benefit of circular k-space coverage of other non-Cartesian SSE strategies such as spirals, rosettes and CRT. This results in a more time-efficient k-space acquisition for a given resolution, as including the corners of k-space (e.g., like in EPSI) cause an anisotropic spatial resolution.⁴⁵ Another advantage of modified rosette trajectories is that they pass through the k-space center in each circumnavigation, which opens the possibility to correct for instabilities such as motion, frequency drifts or gradient delays without the need for additional measurements.46

Limitations 4.1

The gradient amplitudes and slew rates correlate with the compression factors of the modified rosette trajectories. At ultra-high fields $B_0 \ge 7 T$ this can lead to increased gradient hardware stress, which has to be well balanced. Especially beyond 10 T, where higher spectral bandwidths and spatial resolution are expected, this limits the possible SNR gain. Similarly, higher matrix sizes lead to increased slew rates. This could be mitigated by the use of temporal interleaves, which would, however, increase scan times and could—for ¹H MRSI—potentially introduce unwanted spectral artifacts associated with unsuppressed

1522294, 2025, 4, Downloaded from https://onlinelibrary.wiley.com/doi/10.1002/mrm.30368 by Deutsches Zentrum Für Neurodeg, Wiley Online Library on [05/02/2025]. See the Terms and Conditions (https://onlinelibrary.wiley

und-conditions) on Wiley Online Library for rules of use; OA articles are governed by the applicable Creative Commons License

water signals. In general, phantom measurements showed a higher susceptibility of modified rosette trajectories to gradient trajectory errors, if no compensation was used, leading to incorrect signal allocation in the reconstructed image.⁴⁷ However, this problem was fully corrected for by using measured trajectories.

In general, modified rosette and rosette trajectories have longer TAs than SSE approaches like spirals, CRTs and EPSI. This makes them more vulnerable to motion artifacts and less clinically attractive. However, at high-resolution, high-bandwidth 3D coverage, these alternatives are not feasible because of gradient performance limitations. Shen et al. 26,27 showed that using 3D modified rosette trajectories together with CS only 40% of all rosette petals are needed for artifact free images. The possibility of accelerating modified rosette trajectories using CS reconstruction approaches proved useful to a variety of application in recent publications. 48-54 Modified rosette trajectories will likely require a combination with complimentary acceleration methods such as parallel imaging or compressed sensing to reach clinically attractive scan times.

CONCLUSIONS 5

We have shown that high-resolution metabolic mapping using modified rosette trajectories benefits from increased SNR efficiency, whereas staying within the gradient performance limits in comparison to other SSE approaches. Using the two compression parameters, trajectories can be adapted to a variety of applications. This makes rosettes especially interesting for MRSI at ultra-high fields.

ACKNOWLEDGMENTS

This study was funded by Austrian Science Fund (FWF) I 6037-1, FWF P 34198, P36328-N, NIH grant R01EB031787, R01CA255479. M.M. acknowledges the support of the NIH grants P41 EB027061.

CONFLICT OF INTEREST STATEMENT

A.K. is an employee of Siemens Healthineers International AG, Switzerland. The other authors have no conflicts of interest to declare.

ORCID

Małgorzata Marjańska https://orcid.org/0000-0002 -4727-2447

Stanislav Motyka https://orcid.org/0000-0002-6314 -316X

Ovidiu C. Andronesi https://orcid.org/0000-0002-7412 -0641

REFERENCES

- 1. Öz G, Alger JR, Barker PB, et al. Clinical proton MR spectroscopy in central nervous system disorders. Radiology. 2014;270:658-679. doi:10.1148/radiol.13130531
- 2. Maudsley AA, Andronesi OC, Barker PB, et al. Advanced magnetic resonance spectroscopic neuroimaging: Experts' consensus recommendations. NMR Biomed. 2021;34:e4309. doi:10.1002/nbm.4309
- 3. Li Y, Jakary A, Gillung E, et al. Evaluating metabolites in patients with major depressive disorder who received mindfulness-based cognitive therapy and healthy controls using short echo MRSI at 7 tesla. Magn Reson Mater Phys Biol Med. 2016;29:523-533. doi:10.1007/s10334-016-0526-7
- Wang AM, Pradhan S, Coughlin JM, et al. Assessing brain metabolism with 7-T proton magnetic resonance spectroscopy in patients with first-episode psychosis. JAMA Psychiatry. 2019;76:314-323. doi:10.1001/jamapsychiatry.2018.3637
- 5. Hangel G, Cadrien C, Lazen P, et al. High-resolution metabolic imaging of high-grade gliomas using 7T-CRT-FID-MRSI. NeuroImage Clin. 2020;28:102433. doi:10.1016/j.nicl.2020 .102433
- 6. Henning A, Fuchs A, Murdoch JB, Boesiger P. Slice-selective FID acquisition, localized by outer volume suppression (FIDLOVS) for ¹ H-MRSI of the human brain at 7 T with minimal signal loss. NMR Biomed. 2009;22:683-696. doi:10.1002 /nbm.1366
- 7. Nassirpour S, Chang P, Henning A. High and ultra-high resolution metabolite mapping of the human brain using 1H FID MRSI at 9.4T. Neuroimage. 2018;168:211-221. doi:10.1016/j .neuroimage.2016.12.065
- 8. Bogner W, Gruber S, Trattnig S, Chmelik M. High-resolution mapping of human BRAIN metabolites by free induction decay 1H MRSI at 7 T: 1H FID MRSI IN THE HUMAN BRAIN AT 7 T. NMR Biomed. 2012;25:873-882. doi:10.1002/nbm.1805
- 9. Pohmann R, Von Kienlin M, Haase A. Theoretical evaluation and comparison of fast chemical shift imaging methods. J Magn Reson. 1997;129:145-160. doi:10.1006/jmre.1997.1245
- 10. Matsui S, Sekihara K, Kohno H. Spatially resolved nmr spectroscopy using phase-modulated spin-echo trains. J Magn Reson. 1969;67:476-490. doi:10.1016/0022-2364(86)90385-9
- 11. Posse S, DeCarli C, Bihan DL. Three-dimensional echo-planar MR spectroscopic imaging at short echo times in the human brain. Radiology. 1994;192:733-738. doi:10.1148/radiology.192.3 .8058941
- 12. Adalsteinsson E, Irarrazabal P, Topp S, Meyer C, Macovski A, Spielman DM. Volumetric spectroscopic imaging with spiral-basedk-space trajectories. Magn Reson Med. 1998;39:889-898. doi:10.1002/mrm.1910390606
- 13. Bogner W, Hess AT, Gagoski B, et al. Real-time motion- and B0-correction for LASER-localized spiral-accelerated 3D-MRSI of the brain at 3T. Neuroimage. 2014;88:22-31. doi:10.1016/j .neuroimage.2013.09.034
- 14. Schirda CV, Tanase C, Boada FE. Rosette spectroscopic imaging: optimal parameters for alias-free, high sensitivity spectroscopic imaging. J Magn Reson Imaging. 2009;29:1375-1385. doi:10.1002/jmri.21760
- 15. Schirda CV, Zhao T, Andronesi OC, et al. In vivo brain rosette spectroscopic imaging (RSI) with LASER excitation, constant gradient strength readout, and automated LCModel

- quantification for all voxels. *Magn Reson Med.* 2016;76:380-390. doi:10.1002/mrm.25896
- 16. Schirda CV, Zhao T, Yushmanov VE, et al. Fast 3 D rosette spectroscopic imaging of neocortical abnormalities at 3 T: assessment of spectral quality. *Magn Reson Med.* 2018;79:2470-2480. doi:10.1002/mrm.26901
- 17. Mahmud SZ, Denney TS, Bashir A. High-resolution proton metabolic mapping of the human brain at 7 T using free induction decay rosette spectroscopic imaging. *NMR Biomed*. 2024;37:e5042. doi:10.1002/nbm.5042
- Furuyama JK, Wilson NE, Thomas MA. Spectroscopic imaging using concentrically circular echo-planar trajectories in vivo. *Magn Reson Med.* 2012;67:1515-1522. doi:10.1002/mrm.23184
- Chiew M, Jiang W, Burns B, et al. Density-weighted concentric rings k-space trajectory for 1H magnetic resonance spectroscopic imaging at 7 T. NMR Biomed. 2018;31:e3838. doi:10.1002/nbm.3838
- Hingerl L, Bogner W, Moser P, et al. Density-weighted concentric circle trajectories for high resolution brain magnetic resonance spectroscopic imaging at 7T. Magn Reson Med. 2018;79:2874-2885. doi:10.1002/mrm.26987
- 21. Hingerl L, Strasser B, Moser P, et al. Clinical high-resolution 3D-MR spectroscopic imaging of the human brain at 7 T. *Invest Radiol*. 2020;55:239-248. doi:10.1097/RLI.0000000000000626
- 22. Emir UE, Burns B, Chiew M, Jezzard P, Thomas MA. Non-water-suppressed short-echo-time magnetic resonance spectroscopic imaging using a concentric ring *k* -space trajectory. *NMR Biomed.* 2017;30:e3714. doi:10.1002/nbm.3714
- Jiang W, Lustig M, Larson PEZ. Concentric rings K-space trajectory for hyperpolarized ¹³ C MR spectroscopic imaging. *Magn Reson Med*. 2016;75:19-31. doi:10.1002/mrm.25577
- Bogner W, Gagoski B, Hess AT, et al. 3D GABA imaging with real-time motion correction, shim update and reacquisition of adiabatic spiral MRSI. *Neuroimage*. 2014;103:290-302. doi:10.1016/j.neuroimage.2014.09.032
- Bogner W, Otazo R, Henning A. Accelerated MR spectroscopic imaging—a review of current and emerging techniques. NMR Biomed. 2021;34:e4314. doi:10.1002/nbm.4314
- Shen X, Özen AC, Sunjar A, et al. Ultra-short T2 components imaging of the whole brain using 3D dual-echo UTE MRI with rosette k-space pattern. *Magn Reson Med.* 2023;89:508-521. doi:10.1002/mrm.29451
- 27. Shen X, Özen AC, Monsivais H, et al. High-resolution 3D ultra-short echo time MRI with rosette k-space pattern for brain iron content mapping. *J Trace Elem Med Biol.* 2023;77:127146. doi:10.1016/j.jtemb.2023.127146
- Shen X. Development and Applications of 3D Ultra-Short Echo Time MRI with Rosette k-Space Pattern. Purdue University Graduate School; 2022 Accessed January 31, 2024 https://hammer.purdue.edu/articles/thesis/Development_and_Applications_of_3D_Ultra-short_Echo_Time_MRI_with_Rosette_k-Space_Pattern/20323671/1
- 29. Kasper L, Haeberlin M, Dietrich BE, et al. Matched-filter acquisition for bold fMRI. *Neuroimage*. 2014;100:145-160. doi:10.1016/j.neuroimage.2014.05.024
- 30. Pohmann R, Von Kienlin M. Accurate phosphorus metabolite images of the human heart by 3D acquisition-weighted CSI. *Magn Reson Med.* 2001;45:817-826. doi:10.1002/mrm.1110
- Adalsteinsson E, Star-Lack J, Meyer CH, Spielman DM. Reduced spatial side lobes in chemical-shift imaging. Magn Reson Med.

- 1999;42:314-323. doi:10.1002/(SICI)1522-2594(199908)42:2< 314::AID-MRM14>3.0.CO;2-X
- 32. Mareci TH, Brooker HR. Essential considerations for spectral localization using indirect gradient encoding of spatial information. *J Magn Reson.* 1969;92:229-246. doi:10.1016/0022 -2364(91)90267-W
- Greiser A, Von Kienlin M. Efficient k -space sampling by density-weighted phase-encoding. Magn Reson Med. 2003;50:1266-1275. doi:10.1002/mrm.10647
- Kumar Anand C, Ren T, Terlaky T. Optimizing teardrop, an MRI sampling trajectory. *Optim Method Softw.* 2008;23:575-592. doi:10.1080/10556780701874996
- Robson PM, Grant AK, Madhuranthakam AJ, Lattanzi R, Sodickson DK, McKenzie CA. Comprehensive quantification of signal-to-noise ratio and g-factor for image-based and k-space-based parallel imaging reconstructions. *Magn Reson Med*. 2008;60:895-907. doi:10.1002/mrm.21728
- 36. Brodsky EK, Klaers JL, Samsonov AA, Kijowski R, Block WF. Rapid measurement and correction of phase errors from *B* ₀ eddy currents: impact on image quality for non-cartesian imaging. *Magn Reson Med.* 2013;69:509-515. doi:10.1002/mrm.24264
- Robison RK, Li Z, Wang D, Ooi MB, Pipe JG. Correction of B₀ eddy current effects in spiral MRI. Magn Reson Med. 2019;81:2501-2513. doi:10.1002/mrm.27583
- 38. Marques JP, Kober T, Krueger G, Van Der Zwaag W, Van De Moortele PF, Gruetter R. MP2RAGE, a self bias-field corrected sequence for improved segmentation and T1-mapping at high field. *Neuroimage*. 2010;49:1271-1281. doi:10.1016/j.neuroimage.2009.10.002
- 39. Bilgic B, Chatnuntawech I, Fan AP, et al. Fast image reconstruction with L2-regularization. *J Magn Reson Imaging*. 2014;40:181-191. doi:10.1002/jmri.24365
- Provencher SW. Estimation of metabolite concentrations from localizedin vivo proton NMR spectra. Magn Reson Med. 1993;30:672-679. doi:10.1002/mrm.1910300604
- 41. Považan M, Hangel G, Strasser B, et al. Mapping of brain macromolecules and their use for spectral processing of 1 H-MRSI data with an ultra-short acquisition delay at 7 T. *Neuroimage*. 2015;121:126-135. doi:10.1016/j.neuroimage.2015.07.042
- 42. Kreis R, Boer V, Choi I, et al. Terminology and concepts for the characterization of in vivo MR spectroscopy methods and MR spectra: background and experts' consensus recommendations. *NMR Biomed*. 2021;34:e4347. doi:10.1002/nbm.4347
- 43. Lin A, Andronesi O, Bogner W, et al. Minimum reporting standards for in vivo magnetic resonance spectroscopy (MRSin-MRS): Experts' consensus recommendations. *NMR Biomed*. 2021;34:e4484. doi:10.1002/nbm.4484
- 44. Reeder SB, Wintersperger BJ, Dietrich O, et al. Practical approaches to the evaluation of signal-to-noise ratio performance with parallel imaging: application with cardiac imaging and a 32-channel cardiac coil. Magn Reson Med. 2005;54:748-754. doi:10.1002/mrm.20636
- 45. Maudsley AA, Matson GB, Hugg JW, Weiner MW. Reduced phase encoding in spectroscopic imaging. *Magn Reson Med.* 1994;31:645-651. doi:10.1002/mrm.1910310610
- Pipe JG. Motion correction with PROPELLER MRI: application to head motion and free-breathing cardiac imaging. Magn Reson Med. 1999;42:963-969. doi:10.1002/(SICI)1522-2594(199911)42:5<963::AID-MRM17>3.0.CO;2-L

- 47. Patch SK. K-space data preprocessing for artifact reduction in MR. *Imaging*. 2005;1:73-87.
- Bozymski B, Shen X, Özen A, et al. Ultra-short Echo time 31P 3D MRSI at 3T with novel rosette k-space trajectory. Proceedings 30th Scientific Meeting, International Society for Magnetic Resonance in Medicine; ISMRM; 2023:1783. doi:10.58530/2022 /1783
- Farley N, Bozymski B, Dydak U, Emir U. Fast 3D-P31-MRSI using custom rosette petal trajectory at 3T with 4x accelerated compressed sensing. Proceedings 31st Scientific Meeting, International Society for Magnetic Resonance in Medicine; ISMRM; 2023.
- Joy A, Emir U, Macey PM, Thomas MA. Accelerated Rosette Spectroscopic Imaging with semi-LASER Localization. Proceedings 31st Scientific Meeting, International Society for Magnetic Resonance in Medicine; ISMRM; 2023:3953.
- 51. Joy A, Emir U, Macey PM, Thomas MA. Accelerated four-dimensional rosette J-resolved spectroscopic imaging (4D ROSE- JRESI) with semi-LASER localization: a pilot study. Proceedings 31st Scientific Meeting, International Society for Magnetic Resonance in Medicine; ISMRM; 2023:4651.
- 52. Bozymski B, Xin S, Ozen A, et al. Comparison of compressed sensing accelerated rosette UTE and Conventional 31P 3D MRSI at 3T in leg muscle. *Proceedings 31st Scientific Meeting, International Society for Magnetic Resonance in Medicine*; ISMRM; 2023:4643.
- 53. Villarreal C, Shen X, Ozen A, et al. Compressed sensing and the use of 3D UTE acquisition for high-resolution accelerated 23NA imaging at 3T. *Joint Annual Meeting ISMRM-ESMRMB ISMRT 31st Annual Meeting*; ISMRM; 2023:1495. doi:10.58530/2022/1495
- 54. Li Y, Yang R, Zhang C, Zhang J, Jia S, Zhou Z. Analysis of generalized rosette trajectory for compressed sensing MRI. *Med Phys.* 2015;42:5530-5544. doi:10.1118/1.4928152

SUPPORTING INFORMATION

Additional supporting information may be found in the online version of the article at the publisher's website.

Figure S1. Distribution of petals in k-space of the sequences compared (top row). In the bottom row the analytic and measured k-space trajectory can be observed for the petal with rotation angle $\alpha = \pi$ (red box in the top row). **Figure S2.** LCModel control file from an exemplary voxel. **Figure S3.** Resolution phantom experiments with the in vivo protocol. Pixel intensities along a horizontal line in the center of the image are shown below. Comparable

Figure S4. Whole-brain CRLB maps of the metabolites shown in Figure 7.

trajectories.

resolution capabilities can be observed for all compared

Figure S5. Boxplot showing the increase in SNR per-unit-time for the modified rosette trajectories compared to the rosette. The results of the phantom and in vivo measurements are shown.

Table S1. Minimum Reporting Standards for in vivo MR Spectroscopy Note. – Parameters 7 TDMI, CRLB = Cramér-Rao lower bounds; FID = free induction decay; FOV = field of view; SNR = signal-to-noise ratio; VOI = volume of interest.

Table S2. Results of the SNR per-unit-time calculation for the rosette trajectory and modified rosette trajectories from the phantom measurement. SNR values are displayed as the percentage difference from the rosette trajectory. The mean and standard error over all three measurements are shown.

How to cite this article: Blömer S, Hingerl L, Marjańska M, et al. Proton-free induction decay MRSI at 7 T in the human brain using an egg-shaped modified rosette K-space trajectory. *Magn Reson Med.* 2025;93:1443-1457. doi: 10.1002/mrm.30368